Second-order monopile wave loads at linear cost

Bredmose, H.; Pegalajar-Jurado, A.

Published in:
Coastal Engineering

Link to article, DOI:
10.1016/j.coastaleng.2021.103952

Publication date:
2021

Document Version
Peer reviewed version

Journal Pre-proof

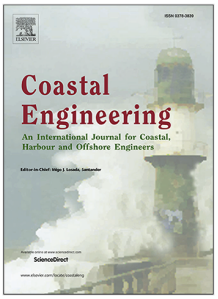

Second-order monopile wave loads at linear cost

H. Bredmose, A. Pegalajar-Jurado

PII: S0378-3839(21)00109-5
DOI: https://doi.org/10.1016/j.coastaleng.2021.103952
Reference: CENG 103952

To appear in: *Coastal Engineering*

Received date : 21 December 2020
Revised date : 14 June 2021
Accepted date : 21 June 2021

Please cite this article as: H. Bredmose and A. Pegalajar-Jurado, Second-order monopile wave loads at linear cost. *Coastal Engineering* (2021), doi: https://doi.org/10.1016/j.coastaleng.2021.103952.

Second-order monopile wave loads at linear cost

H. Bredmose and A. Pegalajar-Jurado

DTU Wind Energy, Nils Koppels Allé Building 403, DK-2800 Kgs. Lyngby, Denmark

Abstract

A method to compute the second-order free surface elevation, depth integrated force and mud line moment for a slender circular vertical cylinder is presented. The method is valid for unidirectional irregular waves and includes inertia loads and viscous loads.

We first derive the linear transfer functions for free surface elevation, depth-integrated force and moment from the complex Fourier amplitudes of the velocity potential. Next, the second-order contributions are expressed through closed form quadratic transfer functions, which are further diagonalized through eigen decomposition. Hereby the second-order contributions can be computed as products of pseudo time series calculated by FFT, with the eigenvectors acting as transfer functions on the linear Fourier ampltitudes.

For a sample 3-hour sea state, we find that eight modes are sufficient to achieve an accuracy of 1% for the maximum peak value of force and moment and 1.3% for free surface elevation, relative to the standard deviation of each signal. These results are obtained 2500 faster than with the conventional approach and we demonstrate that the computational effort of the new method scales like $O(N \log N)$, similar to linear wave loads, where N is the number of frequencies. For the eight mode approximation, the error bound of 1% for loads and 4% for free surface elevation are found to hold across various values of the normalized peak wave number from shallow to deep water. The accuracy is adjustable through the number of modes and is found to be independent of the time series length. The methods potential in practical design is discussed.

Keywords:

1. Introduction

Wave loads on marine structures are the result of stochastic realisations in various sea states over the full life time. Hence, both for fatigue and ULS calculations, an efficient computation of long time series is beneficial. Through Fast Fourier Transforms (FFT), linear methods can be calculated at an effort of $O(N \log N)$, where N is the number of linear wave frequencies. Since this, in turn, is proportional to the time series length, the computational effort scales as the length of the time series. Linear methods, however, are not always

sufficiently accurate for design. First, the peak loads values are usually underpredicted due the missing higher-order corrections, and second, the nonlinear load contributions at the super and sub harmonic frequencies outside the linear spectrum are not included. Recent examples of these effects are given in Suja-Thauvin et al. (2020), Pierella et al. (2021) and Wang et al. (2021). For design of offshore wind turbine substructures, the IEC61400-3-1 (2019) standard thus requires to take nonlinear kinematics into account for the ULS loads.

Offshore wind turbines in the 10-15 MW class typically have natural periods in the range of 4.5–5.5 s and can thus be resonantly excited by second-harmonic force components from waves with the double period and third-harmonic forcing from waves of the triple period. The latter has been the motivation for development of third-order forcing methods to predict 'ringing' response accurately (Grue and Huseby, 2002). Fully nonlinear wave kinematics can be combined with a slender-body force model to calculate such loads, as demonstrated by Schløer et al. (2016) and Wang et al. (2021) for 5 MW and 10 MW turbine configurations. The computational expense of the kinematics computation may be circumvented by use of pre-calculated data bases, as recently presented by Pierella et al. (2020).

The slender body approach for load calculation is valid for diameter to wave length ratios of $D/L < 0.2$ due to the neglection of diffraction (Isaacson, 1979). The balance between inertia and drag loads is governed by the Keulegan-Carpenter number, which is limited by the maximum wave height to take a largest value of $KC_{\max} = 0.44/(D/L)$ (Isaacson, 1979). For a pile of 8m diameter at 33 m depth, the diffraction limit corresponds to a wave period of 5.1s with $KC_{\max} = 2.2$ and thus inertia dominated loads. For a 10 s wave, we have $D/L = 5.7 \cdot 10^{-2}$ and $KC_{\max} = 7.7$. In this regime, the drag loads are therefore contributing for large waves and the limited accuracy of linear wave kinematics can affect the loads.

Despite the lower accuracy, relative to fully nonlinear wave forcing, second-order wave theory is convenient due to its closed form nature and offers a welcome improvement over linear theory. This is utilized in the standard method of Sharma and Dean (1981) which combines Stokes second-order irregular wave theory with the slender body Morison equation (Morison et al., 1950). The second-order kinematics are obtained through double sums that span all frequency pairs. A straight-forward time loop-based implementation will thus result in an $O(N^3)$ effort, but initial grouping of the double sum terms after their output frequency and subsequent utilization of FFT can reduce this effort to $O(N^2)$. This, however, can still be expensive for long time series and often limits the practical application of second-order force calculations in design. The aim of the present paper is therefore to achieve a second-order load method which can be evaluated at an effort of $O(N \log N)$, similarly to linear loads. This could potentially lift the accuracy in standard Engineering calculations from first to second order.

Several examples of rapid second-order methods exist in the literature. For instance, the squared velocity term of the Bernoulli equation can be computed at $O(N \log N)$ by direct multiplication of FFT-generated time series. Time

domain products have also been utilised in the context of second-order wave models for the spatial evolution of the free surface Fourier coefficients by Bredmose et al. (2004) and Bredmose et al. (2005). In the context of second-order Stokes theory, Walker et al. (2004) introduced a narrow-band approximation for the second-order free surface elevation, where the interaction coefficient for an optimised fixed non-dimensional wave number is used to approximate the full super harmonic contribution in the time domain. In a later study, Taylor et al. (2007) pointed out the quadratic transfer function (QTF) for the super harmonic free surface elevation of a four column structure was to a large extent dominated by its dependence to the sum frequency of the interacting frequency pairs. This would allow for an approximate representation by its diagonal and relates to the Newman approximation (Newman, 1974) for the low-frequency drift forces of offshore structures. In this widely used approximation, the diagonal of the sub harmonic force QTF is utilized to approximate the full QTF. If further combined with the proposed modification of Standing et al. (1987), the approximate QTF matrix can be written as an outer product of a column and a row vector, and the low-frequency forcing be obtained as a time domain product. One further way to speed up load calculations for slender bodies is to replace the numerical integration along the structure with its closed-form analytical result. This has been applied at second order by Kim and Chen (1994) for difference frequency inertia loads in directional seas and by Dean and Dalrymple (1991) for the drag loads of regular waves.

In the current work, we focus on unidirectional second-order irregular Stokes waves and their loads on slender monopiles. We adopt the force model of Rainey (1995), extended with the standard viscous drag term of the Morison equation. By use of double-sided Fourier series and analytical depth integration, we are able to provide closed form expressions for the force, moment and free surface elevation QTFs. We next diagonalize the QTFs through eigenvalue decomposition to allow evaluation of the second-order contributions through FFT. The numerical cost of the eigen decomposition is kept small by the use of a relatively coarse grid and subsequent interpolation within the resulting eigenvectors. Finally, the $O(N \log N)$ scaling is achieved through modal truncation. Initial results of the method have been reported in Bredmose and Pegalajar-Jurado (2020). We here present the full study with detailed derivation, extension to free surface elevation and error analysis. Generalized QTF formulae for a vertical cylinder truncated at arbitrary vertical levels are provided as an appendix.

The governing equations and force model are presented in section 2, followed by the linear solution and non-dimensionalization in section 3. The second-order force and the speed-up method is next described in section 4, followed by the expressions for moment and free surface elevation in section 5. The accuracy and efficiency of the method is investigated in sections 6–7 and finally a summary and discussion is provided in section 8.

2. Problem formulation

We consider a vertical circular cylinder of diameter D at a depth h. A Cartesian coordinate system is adopted with the vertical z-axis pointing upwards from the still water level at the cylinder center and the x-axis pointing in the direction of wave propagation.

The free surface elevation, η, is measured upwards from the still water level. Further, the horizontal and vertical fluid velocities are expressed by a velocity potential such that $(u, w)^T = \nabla\phi$. The incident waves are governed by the following equations

$$\nabla^2\phi = 0 \qquad -h < z < \eta \tag{1}$$

$$\phi_z = 0 \qquad z = -h \tag{2}$$

$$\eta_t + \nabla_H\phi \cdot \nabla\eta - \phi_z = 0 \qquad z = \eta \tag{3}$$

$$\phi_t + g\eta + \tfrac{1}{2}\left(\nabla\phi \cdot \nabla\phi\right) = C(t) \qquad z = \eta, \tag{4}$$

which express mass conservation, impermeability of the sea bed and the kinematic and dynamic free-surface boundary conditions. Here $\nabla_H = (\partial_x, \partial_y)^T$ denotes the gradient operator in the horizontal plane and $C(t)$ is the Bernoulli constant, which in potential flow theory is a function of time only. Following classical Stokes wave theory (e.g. Fenton, 1985), the free surface conditions can be Taylor expanded around the still water level at $z = 0$. It is here practical to define $\Phi = \phi|_{z=0}$. Further, by repeated use of $\Phi_{zz} = -\nabla_H^2\Phi$ and the leading-order relations $\Phi_z = \eta_t = -\Phi_{tt}/g$,$\eta = -\Phi_t/g$, the following form of the free surface conditions at $z = 0$ can be obtained

$$\Phi_{tt} + g\Phi_z = -\left(\nabla_H\Phi \cdot \nabla_H\Phi\right)_t - \frac{1}{g^2}\left(\Phi_{tt}^2\right)_t - \frac{1}{g^2}\Phi_{tttt}\Phi_t - \nabla_H^2\Phi\Phi_t \tag{5}$$

$$\eta = -\frac{1}{g}\Phi_t - \frac{1}{2g}\left(\nabla_H\Phi \cdot \nabla_H\Phi + \frac{1}{g^2}\Phi_{tt}^2\right) - \frac{1}{g^3}\Phi_{ttt}\Phi_t + C/g. \tag{6}$$

We shall pursue a solution to these equations where η and Φ can be expressed as trigonometric sums in time and space with a zero mean value. It turns out that $C(t)$ can then be constant in time and its value be defined through the requirement that the mean value of η in (6) is zero. This approach is similar to the one of Fenton (1985) and avoids the need to introduce a set down for η; a constant value of Φ_t or an elevated origin of the coordinate system.

2.1. Force formulation and a preview of first- and second-order results

The horizontal force and moment on the cylinder are obtained by depth-integration of the inertia force as formulated by Rainey (1995) and the standard Morison et al. (1950) viscous force,

$$\begin{pmatrix} F \\ M \end{pmatrix} = \int_{-h}^{\eta} \rho\tfrac{\pi}{4}D^2\left[\left(C_a + 1\right)\dot{u} + C_a w_z u\right]\begin{pmatrix} 1 \\ z \end{pmatrix}\mathrm{d}z + \int_{-h}^{\eta} \rho D C_d u|u|\begin{pmatrix} 1 \\ z \end{pmatrix}\mathrm{d}z. \tag{7}$$

Here ρ is the water density, C_a is the added mass coefficient, C_d is the drag coefficient, and u and w are the horizontal and vertical wave particle velocities, respectively. The subscript $\square_z$ indicates spatial derivative in the vertical direction. We consider a cylinder that reaches from the free surface at $z = \eta$ to the sea bed at $z = -h$, while formulae for the generalization to a cylinder that spans between two fixed z-levels are given in the appendix. This latter generalization can be used for e.g. spar floaters, see Pegalajar-Jurado and Bredmose (2020). In comparison to the simplest Morison inertia load, which is based on the Eulerian horizontal particle acceleration u_t, the Rainey force model is based on the Lagrangian particle acceleration $\dot{u}$ and includes further the axial divergence term, which accounts for the non-slenderness of the cylinder in the vertical direction. The recent force model of Kristiansen and Faltinsen (2017) is identical to the Rainey model for the wetted part of the cylinder in the case of circular cross sections. Both of these force models include a point load at the free surface which is not included here due to its third-order magnitude. A recent study by Suja-Thauvin et al. (2020) suggested that although these two point loads appear to differ by a factor of 8, their third-harmonic force for large-amplitude regular waves are remarkably close.

We now divide the wave field into its first- and a second-order parts, assuming a small value of ka where k is the wave number and a is a representative wave amplitude:

$$\eta = \eta_1 + \eta_2 \tag{8}$$

$$\Phi = \Phi_1 + \Phi_2 \tag{9}$$

$$\begin{pmatrix} u \\ w \end{pmatrix} = \begin{pmatrix} u \\ w \end{pmatrix}_1 + \begin{pmatrix} u \\ w \end{pmatrix}_2 = \nabla\phi = \nabla\phi_1 + \nabla\phi_2. \tag{10}$$

The force can hereby be decomposed into its linear part

$$F_1 = \rho \tfrac{\pi}{4} D^2 \left(C_a + 1\right) \int_{-h}^{0} u_{1,t} \, \mathrm{d}z \tag{11}$$

and its second-order part

$$F_2 = \underbrace{\rho\tfrac{\pi}{4}D^2\left(C_a+1\right)\int_{-h}^{0} u_{2,t}\ \mathrm{d}z}_{F_{21}} \tag{12}$$

$$+\underbrace{\rho\tfrac{\pi}{4}D^2\left(C_a+1\right)\int_{-h}^{0}\left(u_1u_{1,x}+w_1u_{1,z}\right)\ \mathrm{d}z}_{F_{22}} \tag{13}$$

$$+\underbrace{\rho\tfrac{\pi}{4}D^2C_a\int_{-h}^{0} w_{1,z}u_1\ \mathrm{d}z}_{F_{23}}+\underbrace{\rho\tfrac{\pi}{4}D^2\left(C_a+1\right)\eta_1u_{1,t}|_{z=0}}_{F_{24}} \tag{14}$$

$$+\underbrace{\tfrac{1}{2}\rho DC_d\int_{-h}^{0} u_1|u_1|\ \mathrm{d}z}_{F_{25}}. \tag{15}$$

Here the subscripts $\square_1$ and $\square_2$ denote the first- and second-order component of a given quantity, whereas the subscripts (x, z, t) indicate differentiation with respect to these variables. The linear part is seen to result from the first-order Eulerian acceleration, while the second-order force results from the second-order Eulerian acceleration (F_{21}), the convective acceleration (F_{22}), the axial divergence force (F_{23}), the leading-order contribution from integration above the still water level (F_{24}) and the viscous drag force (F_{25}). All terms except for (F_{21}) are expressed by the first-order velocity field and integration is carried out between the sea bed and the still water level. A similar decomposition of the moment can be made.

An example of the first-order alone (S&D 1) and first-order plus second-order (S&D 1+2) solution is given in figure 1. The plots show free surface elevation, force and moment for a NewWave wave group (Tromans et al., 1991) at $h = 33$ m depth for a JONSWAP spectrum of peak period $T_p = 10$ s and with a peak enhancement parameter of $\gamma = 3.3$. A pile diameter of $D = 8$ m was chosen with generic force coefficients of $C_a = C_d = 1.0$ and a water density of $\rho = 1025$ kg/m^3. The wave kinematics was calculated with the Sharma and Dean (1981) wave theory and depth-integrated numerically with 40 points along the pile. The figure shows how the second-order correction narrows the crest and lifts both the crest and trough. The force and mudline moment become steeper and more asymmetric by the inclusion of the second-order terms. Quantitatively, the second-order contribution adds 21.9%, 32.2% and 60.1% to the peak values of the linear free-surface elevation, force and moment, respectively. We note that these numbers are specific to the example shown here, as the second-order contributions grow with the square of the wave amplitude.

A closer inspection of the various terms in (12) is offered by figure 2, in terms of the mudline moment. The double frequency content of M_{21}–M_{24} is clearly seen. We further see that the contributions of M_{21}–M_{23} are more or less equal in magnitude at 20–30 MNm, while the drag contribution is slightly

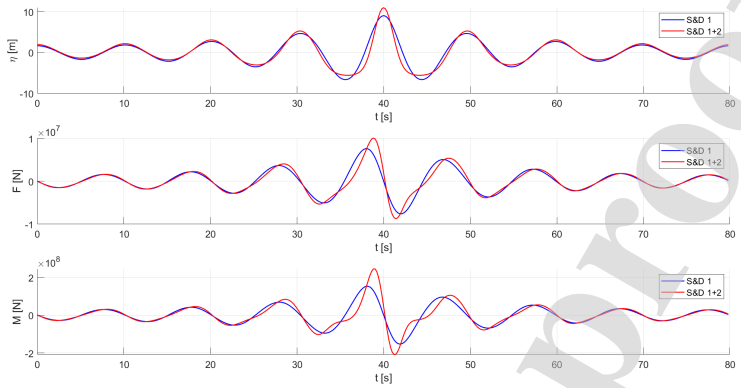

Figure 1: Free surface elevation, inline force and mudline moment for a NewWave group at 33m depth.

larger (40 MNm) and the point force from integration above the still water level dominates the second-order moment through its value of 100 MNm. Although a similar tendency occurs for the inline force, the moment contribution is exaggerated by the long arm for the point load, acting entirely at the still water level.

The figure shows the results calculated through the Sharma and Dean (1981) theory as red dots. The underlying blue curve results from the approximate, accelerated method which is the target of the present paper. At the graphical level, the approximate method is seen to compare well. We will detail the method in the following sections and document its accuracy and efficiency in section 7.

3. First-order solution and normalization

The first-order problem emerges when (8)–(10) are substituted into (1)–(4). The linear incident wave potential satisfies (1)–(2) and the homogeneous version of (5). The solution can be written as the double sided Fourier series

$$\phi_1 = \sum_{j=-N}^{N} \hat{B}_j \mathrm{e}^{\mathrm{i}(\omega_j t - k_j x)} \frac{\cosh k_j(z+h)}{\cosh k_j h} \tag{16}$$

where N is the number of positive frequencies, t is time and $\omega_j = j\omega_1$ are the angular frequencies. To make the Fourier series real, we further impose the conditions $\hat{B}_{-j} = \hat{B}_j^*$ and $k_{-j} = -k_j$. Here * indicates the complex conjugate and k_j are the wave numbers, which satisfy the linear dispersion relation

$$\omega_j^2 = g k_j \tanh k_j h. \tag{17}$$

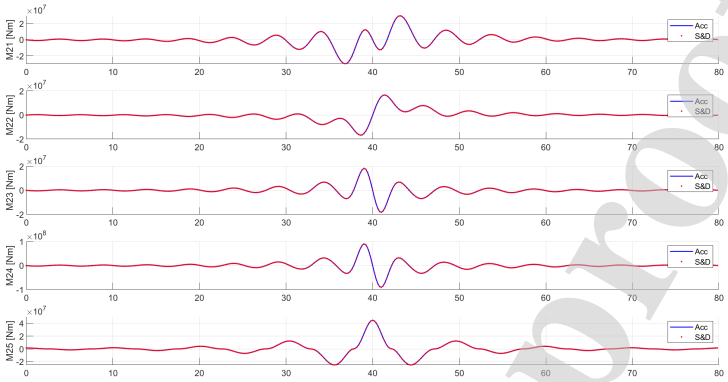

Figure 2: The second-order moment contributions for the NewWave group of figure 1.

The similar solution for η_1 reads

$$\eta_1 = \sum_{j=-N}^{N} \hat{A}_j \mathrm{e}^{\mathrm{i}(\omega_j t - k_j x)}, \tag{18}$$

where $\hat{A}_{-j} = \hat{A}_j^*$ and where the complex Fourier amplitudes $(\hat{A}_j, \hat{B}_j)$ are related through (6) as follows

$$\hat{B}_j = \mathrm{i}\frac{g}{\omega_j}\hat{A}_j. \tag{19}$$

The first-order force (11) is now easily calculated by integration of $u_{1,t} = \nabla\phi_{1,t}$

$$F_1 = \rho\tfrac{\pi}{4}D^2\,(C_a+1)\int_{-h}^{0} \nabla\phi_{1,t}\,\mathrm{d}z \tag{20}$$

$$= \rho\tfrac{\pi}{4}D^2\,(C_a+1)\sum_{j=-N}^{N}\left[\hat{B}_j \mathrm{e}^{\mathrm{i}(\omega_j t - k_j x)}(\mathrm{i}\omega_j)(-\mathrm{i}k_j)\int_{-h}^{0}\frac{\cosh k_j(z+h)}{\cosh k_j h}\,\mathrm{d}z\right] \tag{21}$$

$$= \rho\tfrac{\pi}{4}D^2\,(C_a+1)\sum_{j=-N}^{N}\left[\hat{B}_j \mathrm{e}^{\mathrm{i}(\omega_j t - k_j x)}\omega_j \tanh k_j h\right] \tag{22}$$

We can further express the force in non-dimensional form through normalization with h, g and R. To this end we introduce the dimensionless variables

$$\Omega = \omega\sqrt{h/g} \quad , \qquad \kappa = kh \tag{23}$$

$$\tilde{\phi} = \phi\; h^{-3/2}g^{-1/2} \quad , \qquad \hat{\tilde{B}} = \hat{B}\; h^{-3/2}g^{-1/2} \tag{24}$$

$$\tilde{\eta} = \eta/h \quad , \qquad \hat{\tilde{A}} = \hat{A}/h. \tag{25}$$

The dimensionless version of the transfer function between the amplitudes of potential and free surface elevation (19) can then be written as

$$\hat{\tilde{B}} = \frac{\mathrm{i}}{\Omega}\hat{\tilde{A}}, \tag{26}$$

and the linear force can be expressed as

$$\frac{F_1}{\rho g \pi R^2 h} = \sum_{j=-N}^{N} (C_a + 1)\mathcal{F}_1 \hat{\tilde{B}}_j \mathrm{e}^{\mathrm{i}(\omega_j t - k_j x)} \tag{27}$$

with the force transfer function

$$\mathcal{F}_1 = \Omega \tanh \kappa. \tag{28}$$

The moment around the still water level, M_{SWL}, can be obtained in the same way as for the force. It relates to the mud line moment M_b through

$$M_b = M_{\mathrm{SWL}} + Fh \tag{29}$$

where F is the force. We shall exclude the 'SWL' subscript to keep a clear notation, such that unless other is specified, the moments are calculated around $z = 0$. The linear moment can now be calculated by integration, similarly to the linear force

$$M_1 = \rho\pi R^2 (C_a + 1) \int_{-h}^{0} u_{1,t} z \, \mathrm{d}z \tag{30}$$

$$= \rho\pi R^2 (C_a + 1) \sum_{j=-N}^{N} \frac{k_j \omega_j}{\cosh k_j h} \hat{B}_j \int_{-h}^{0} \cosh(k_j(z+h)) \, z \, \mathrm{d}z \, \mathrm{e}^{\mathrm{i}(\omega_j t - k_j x)} \tag{31}$$

$$= \rho\pi R^2 (C_a + 1) \sum_{j=-N}^{N} \hat{B}_j \frac{\omega_j}{k_j} \left(\frac{1}{\cosh k_j h} - 1 \right) \mathrm{e}^{\mathrm{i}(\omega_j t - k_j x)}. \tag{32}$$

This leads to the non-dimensional transfer function for the moment

$$\frac{M_1}{\rho g \pi R^2 h^2} = (C_a + 1) \sum_{j=-N}^{N} \mathcal{M}_1 \hat{\tilde{B}}_j \, \mathrm{e}^{\mathrm{i}(\omega_j t - k_j x)} \quad , \quad \mathcal{M}_1 = \frac{\Omega}{\kappa} \left(-1 + 1/\cosh \kappa \right). \tag{33}$$

4. The second-order force and the speed-up method

The second-order force is defined in (12). We now derive a compact quadratic force transfer function and show how its computation can be speeded up by eigenvalue decomposition and FFTs. We start out with the contribution from F_{21}.

4.1. The inertia force from the second-order incident wave field F_{21}

The inertia force F_{21} is similar to the linear inertia force, but is associated with the second-order potential. This is readily derived by insertion of (9) into (5), whereby one gets

$$\tilde{\phi}_2 = \mathrm{i} \sum_{m=-N}^{N} \sum_{n=-N}^{N} \hat{\tilde{B}}_m \hat{\tilde{B}}_n \mathcal{T}_\Phi \mathrm{e}^{\mathrm{i}((\omega_m+\omega_n)t-(k_m+k_n)x)} \frac{\cosh(k_m+k_n)(z+h)}{\cosh(k_m+k_n)h} \tag{34}$$

with

$$\mathcal{T}_\Phi = \frac{1}{2} \frac{2(\Omega_m+\Omega_n)\left(\Omega_m^2\Omega_n^2 - \kappa_m\kappa_n\right) + \Omega_m\left(\Omega_n^4 - \kappa_n^2\right) + \Omega_n\left(\Omega_m^4 - \kappa_m^2\right)}{\left(\Omega_m+\Omega_n\right)^2 - \left(\kappa_m+\kappa_n\right)\tanh\left(\kappa_m+\kappa_n\right)}. \tag{35}$$

This result is consistent with Sharma and Dean (1981) and Madsen and Fuhrman (2006). Similar to Schäffer and Steenberg (2003), though, we have utilized the complex exponential function with complex Fourier amplitudes, to avoid explicit phase angles or combinations of both cosine and sine functions in the first- and second-order expressions. One further simplification is achieved by the double-sided format of the Fourier sums. This eliminates the need to distinguish between sub- and super harmonic interaction kernels, since both are implicitly represented in the double sum multiplication.

The inertia force from the second-order wave field is now obtained in the same way as the linear force through integration of the $\nabla\phi_{2,t}$. We hereby obtain

$$\frac{F_{21}}{\rho g \pi R^2 h} = (C_a+1)\mathrm{i} \sum_{m=-N}^{N} \sum_{n=-N}^{N} \hat{\tilde{B}}_m \hat{\tilde{B}}_n \mathcal{F}_{21} \mathrm{e}^{\mathrm{i}((\omega_m+\omega_n)t-(k_m+k_n)x)} \tag{36}$$

with

$$\mathcal{F}_{21} = \mathcal{T}_\Phi \left(\Omega_m+\Omega_n\right)\tanh\left(\kappa_m+\kappa_n\right). \tag{37}$$

We can compute this efficiently by writing (36) as a matrix-vector product and next utilize the eigenvalue diagonalization of the $\mathcal{F}_{21}$ interaction matrix, which

is symmetric and real:

$$\frac{F_{21}}{\rho g \pi R^2 h} = (C_a+1)\mathrm{i}\left[\ldots \hat{\tilde{B}}_m \mathrm{e}^{\mathrm{i}(\omega_m t - k_m x)} \ldots\right] \mathcal{F}_{21} \begin{bmatrix} \vdots \\ \hat{\tilde{B}}_n \mathrm{e}^{\mathrm{i}(\omega_n t - k_n x)} \\ \vdots \end{bmatrix} \tag{38}$$

$$= (C_a+1)\mathrm{i}\sum_{j=1}^{2N}\left[\ldots \hat{\tilde{B}}_m \mathrm{e}^{\mathrm{i}(\omega_m t - k_m x)} \ldots\right] \mathbf{V_j}\lambda_j \mathbf{V}_j^T \begin{bmatrix} \vdots \\ \hat{\tilde{B}}_n \mathrm{e}^{\mathrm{i}(\omega_n t - k_n x)} \\ \vdots \end{bmatrix} \tag{39}$$

$$= (C_a+1)\,\mathrm{i}\sum_{q=1}^{2N}\lambda_q \left[\sum_{m=-N}^{N} V_{qm}\hat{\tilde{B}}_m \mathrm{e}^{\mathrm{i}(\omega_m t - k_m x)}\right]\left[\sum_{n=-N}^{N} V_{qn}\hat{\tilde{B}}_n \mathrm{e}^{\mathrm{i}(\omega_n t - k_n x)}\right]. \tag{40}$$

Here $(\lambda_j, \mathbf{V}_j)$ are the eigenvalues and eigenvectors of the $\mathcal{F}_{21}$ matrix, sorted after descending magnitude. The matrix is evaluated at all the frequency pairs of the double summation (36) and is thus $2N \times 2N$. In the last line we have collected the products of the Fourier vector and the eigenvector into the bracketed sums and observe that the eigenvector plays the role of a transfer function. These sums can thus be computed by inverse FFT and are formally time series. Next, similar to SVD analysis, we may need only a limited number of them to obtain a suitable approximation for the resulting force. By limiting to a small number of modes, we may thus obtain F_{21} by a finite number of time domain products, where the time series are calculated by FFT. This will lead to an approximate value of F_{21} at a computational cost that scales like $O(N \log N)$, similarly to the linear force computation.

Some further notes on the calculation of (40) are now given. First we observe that the two time series are identical. Hence, the time domain product can be obtained by self-multiplication of just one time series. Next, it has been observed that the eigenvalues are pair-wise identical, although with alternating sign and that the two corresponding eigenvectors satisfy $|V_{1,j}| = |V_{2,2N-j}|$. This allows us to use only every second eigen vector, where multiplication by two and taking the real part yield the full result. The final result can thus be written

$$\frac{F_{21}}{\rho g \pi R^2 h} = (C_a+1)\ 2\Re\left(\mathrm{i}\sum_{q=1,q\ \mathrm{odd}}^{Q}\lambda_q f_{21,q}^2\right), \tag{41}$$

where $f_{21,q}$ is the time series obtained with eigenvector V_j as transfer function,

$$\hat{f}_{21,qj} = \hat{\tilde{B}}_j V_{qj}. \tag{42}$$

Initially SVD decomposition was used instead of eigenvalue decomposition. This approach is also possible, and also showed the pair-wise modes. It does,

however, not lead to identical time series in the time domain product, and thus required two transfer functions per mode instead of one. It was checked for one numerical example, that the approximate quadratic transfer matrices, obtained by summation of $\lambda_q V_q V_q^T$ were identical for mode pairs of the eigenvalue decomposition and SVD decomposition.

Finally, it is noted that in the present format, the quadratic transfer functions are real and functions of the non-dimensional parameters Ω and κ. Hereby also the eigenvector based transfer functions are real and generic due to their independence of structural properties and explicit depth. This provides the last element of the method's numerical efficiency: since the generic eigenvectors are smooth functions of Ω, the quadratic transfer matrices can be eigen decomposed on a coarse frequency grid and the V_{qj} for long time series (finer frequency vector) can next be calculated by interpolation. Thus, although eigenvalue decomposition is an $O(N^2)$ process for a fixed number of eigenpairs, the N is kept small and will not dominate the computational effort for long time series.

4.2. The full force formulation

With inspiration from the above method, the other force components of (12) are expressed in a similar format:

$$\frac{F_I}{\rho g \pi R^2 h} = \mathrm{i} \sum_{m=-N}^{N} \sum_{n=-N}^{N} \left[(C_a + 1) \left(\mathcal{F}_{21} + \mathcal{F}_{22} + \mathcal{F}_{24} \right) + C_a \mathcal{F}_{23} \right] \hat{\bar{B}}_m \hat{\bar{B}}_n \mathrm{e}^{\mathrm{i}((\omega_m + \omega_n)t - (k_m + k_n)x)} \tag{43}$$

$$\frac{F_D}{\rho g \pi R h^2} = \psi(\bar{u}_1) \sum_{m=-N}^{N} \sum_{n=-N}^{N} C_d \mathcal{F}_{25} \hat{\bar{B}}_m \hat{\bar{B}}_n \mathrm{e}^{\mathrm{i}((\omega_m + \omega_n)t - (k_m + k_n)x)}, \tag{44}$$

where $\psi(\bar{u}_1)$ and the interaction coefficients are defined below. It should be noted that F_{22}–F_{25} are products of first-order wave properties which can be computed by linear transfer functions with no significant cost. By utilizing the quadratic format, however, the vertical integration can be carried out explicitly, thus saving computational time and avoiding the error introduced by numerical integration.

We now detail the derivation of the quadratic transfer functions $\mathcal{F}_{22}$–$\mathcal{F}_{25}$. The inertia force from convective acceleration can be written as

$$\frac{F_{22}}{(C_a + 1)\, \rho \pi R^2} = \int_{-h}^{0} \left(u_1 u_{1,x} + w_1 u_{1,z} \right) \, \mathrm{d}z \tag{45}$$

$$= \mathrm{i} \sum_{m=-N}^{N} \sum_{n=-N}^{N} \frac{k_m k_n^2 h \mathrm{IF}_1 - k_m k_n^2 h \mathrm{IF}_2}{\cosh k_m h \ \cosh k_n h} \hat{B}_m \hat{B}_n \mathrm{e}^{\mathrm{i}((\omega_m + \omega_n)t - (k_m + k_n)x)}, \tag{46}$$

with

$$\mathrm{IF}_1 = \frac{1}{h}\int_{-h}^{0} \cosh k_m(z+h)\cosh k_n(z+h)\ \mathrm{d}z = \frac{1}{2}\left(C_1 + C_2\right) \tag{47}$$

$$\mathrm{IF}_2 = \frac{1}{h}\int_{-h}^{0} \sinh k_m(z+h)\sinh k_n(z+h)\ \mathrm{d}z = \frac{1}{2}\left(C_1 - C_2\right) \tag{48}$$

and where

$$C_1 = \frac{\sinh(\kappa_m + \kappa_n)}{\kappa_m + \kappa_n} \quad , \quad C_2 = \frac{\sinh(\kappa_m - \kappa_n)}{\kappa_m - \kappa_n}. \tag{49}$$

For C_1 and C_2, the asymptotic limit of unity must be applied for the case when the denominator is equal to zero. We hereby get

$$\mathcal{F}_{22} = \frac{\kappa_m\kappa_n\left(\kappa_m + \kappa_n\right)}{2\ \cosh\kappa_m\ \cosh\kappa_n}\left(\mathrm{IF}_1 - \mathrm{IF}_2\right). \tag{50}$$

For the axial divergence force, we obtain by similar means

$$\mathcal{F}_{23} = -\frac{\kappa_m\kappa_n\left(\kappa_m + \kappa_n\right)}{2\ \cosh\kappa_m\ \cosh\kappa_n}\mathrm{IF}_1. \tag{51}$$

The surface force F_{24} can be computed directly as a time series product. It can, however, also be written in same format as the other inertia forces. The associated quadratic transfer function is

$$\mathcal{F}_{24} = -\tfrac{1}{2}\Omega_m\Omega_n\left(\kappa_m + \kappa_n\right). \tag{52}$$

The drag force F_D is different in nature to the inertia loads, but is retained here for completeness. Monopile structures are usually inertia dominated, and the drag force is generally out of phase with the inertia force and thus only gives a small contribution to the force peak values. The contribution of the drag to the total loads will be assessed in section 7.

The absolute value for velocity in the drag force term makes the analytical integration infeasible. We overcome this by the approximation

$$F_{25} = \tfrac{1}{2}\rho D C_d \int_{z=-h}^{0} u_1^2\ \mathrm{d}z\ \psi(\bar{u}_1), \tag{53}$$

where

$$\psi(\bar{u}_1) = \tanh\left(3\bar{u}_1/\sigma_{\bar{u}_1}\right) \tag{54}$$

and where $\bar{u}_1$ is the depth-averaged linear horizontal particle velocity and $\sigma_{\bar{u}_1}$ is the standard deviation of the associated time series. This is a smoothed representation of $\psi = \mathrm{sgn}(\bar{u}_1)$. The latter approximation is exact for regular waves and allows the integral to be evaluated in the same way as the other

quadratic terms. Next $\bar{u}_1$ can be calculated by a linear transfer function and the multiplication with the ψ function can be carried out in the time domain.

For irregular wave cases, it can occur that $\bar{u}_1$ and the integral of $u_1|u_1|$ do not change sign at the same instant. In this situation, the approximation of (54) is not valid. An example is shown in figure 3 for a 3-hour realization of the same sea state as in figure 1, approximated with eight effective modes. The significant wave height is $H_s = 10$ m. The event shown is the one with the

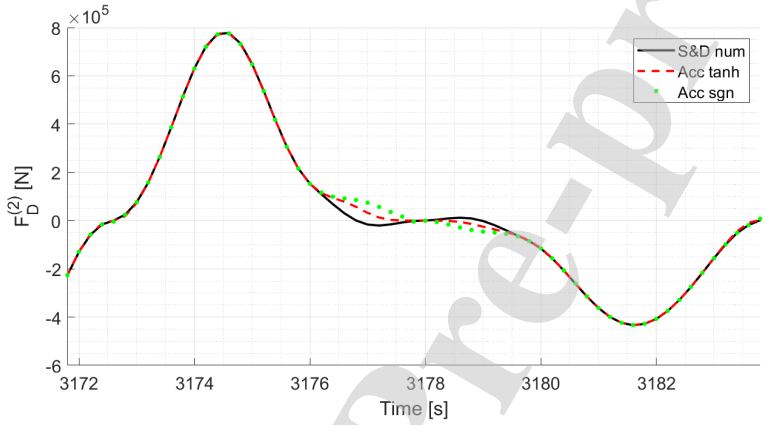

Figure 3: Time series of drag force for a 3-hour irregular sea state and 8 effective modes. The window shows the portion of the signals where the error is maximum.

largest error from the approximation over the realization, and it is seen that the tanh variation of ψ smoothens out the error that the sgn function would introduce. The approximation does not affect the peaks of the drag force, but only introduces some errors where the drag force is close to zero. The factor of 3 inside the tanh function in (54) was found to provide a good balance between smoothness and limited effect on the larger-value parts of the signal.

We can hereby express the drag load also by a quadratic transfer function as follows

$$\mathcal{F}_{25} = -\frac{\kappa_m \kappa_n}{\cosh \kappa_m \ \cosh \kappa_n} \mathrm{IF}_1. \tag{55}$$

For this transfer function no paired nature of the eigenvalues was found and all modes up to the modal truncation value must therefore be included.

5. The second-order moment and free surface elevation

The compact quadratic formulation and speed-up method can readily be applied to the moment and the free surface elevation.

5.1. Second-order moment

We define the moment contributions from each of the force terms of (12), where the only difference is that for the integrals, a moment arm is introduced within each depth integral as an additional factor of z. In line with (43)–(44) we write the total second-order moment as

$$\frac{M_I}{\rho\pi R^2h^2} = \mathrm{i}\sum_{m=-N}^{N}\sum_{n=-N}^{N}\left[(C_a+1)\left(\mathcal{M}_{21}+\mathcal{M}_{22}\right)+C_a\mathcal{M}_{23}\right]\hat{\bar{B}}_m\hat{\bar{B}}_n\mathrm{e}^{\mathrm{i}((\omega_m+\omega_n)t-(k_m+k_n)x)} \tag{56}$$

$$\frac{M_D}{\rho g\pi Rh^3} = \psi(\bar{u}_1)\sum_{m=-N}^{N}\sum_{n=-N}^{N}C_d\mathcal{M}_{25}\hat{\bar{B}}_m\hat{\bar{B}}_n\mathrm{e}^{\mathrm{i}((\omega_m+\omega_n)t-(k_m+k_n)x)} \tag{57}$$

$$\tag{58}$$

where the quadratic transfer functions $\mathcal{M}_{21}$–$\mathcal{M}_{25}$ will be defined in the following. Since F_{24}, the surface force, acts at $z=0$, it has no moment contribution around the still water level.

The quadratic transfer functions are obtained through integration. For the inertia moment from the second-order Eulerian acceleration, the derivation is similar to the integration of the linear moment and we obtain

$$\mathcal{M}_{21} = \mathcal{T}_\phi\frac{\Omega_m+\Omega_n}{\kappa_m+\kappa_n}\left(-1+1/\cosh(\kappa_m+\kappa_n)\right). \tag{59}$$

Next, for the convective acceleration we utilize the results

$$\mathrm{IM}_1 = \frac{1}{h^2}\int_{-h}^{0}\cosh k_m(z+h)\cosh k_n(z+h)\;z\;\mathrm{d}z = -\frac{1}{2}\left(C_3+C_4\right) \tag{60}$$

$$\mathrm{IM}_2 = \frac{1}{h^2}\int_{-h}^{0}\sinh k_m(z+h)\sinh k_n(z+h)\;z\;\mathrm{d}z = -\frac{1}{2}\left(C_3-C_4\right) \tag{61}$$

where

$$C_3 = \frac{\cosh(\kappa_m+\kappa_n)-1}{(\kappa_m+\kappa_n)^2}\quad,\quad C_4 = \frac{\cosh(\kappa_m-\kappa_n)-1}{(\kappa_m-\kappa_n)^2} \tag{62}$$

and where again the limits $C_3=1/2$, $C_4=1/2$ apply when their respective denominators are equal to zero.

We now obtain

$$\mathcal{M}_{22} = \frac{\kappa_m\kappa_n\left(\kappa_m+\kappa_n\right)}{2\;\cosh\kappa_m\;\cosh\kappa_n}\left(\mathrm{IM}_1-\mathrm{IM}_2\right) \tag{63}$$

$$\mathcal{M}_{23} = -\frac{\kappa_m\kappa_n\left(\kappa_m+\kappa_n\right)}{2\;\cosh\kappa_m\;\cosh\kappa_n}\mathrm{IM}_1 \tag{64}$$

$$\mathcal{M}_{25} = -\frac{\kappa_m\kappa_n}{\cosh\kappa_m\;\cosh\kappa_n}\mathrm{IM}_1. \tag{65}$$

As an example, the spectra of the inertia and drag second-order moments for the 3-hour realization of figure 3 are shown in figure 4, again based on eight effective modes. It can be seen that the agreement with the reference solution of Sharma and Dean (1981) is excellent at the spectral level as well. To better understand the frequency content of the moment spectra, the spectrum of the corresponding first-order free-surface elevation is shown in the top panel. As expected, the inertia second-order moment shows significant energy around 0.2 Hz, corresponding to the second harmonic of the wave peak frequency. The drag moment, on the other hand, shows energy mainly around the wave peak frequency (0.1 Hz), and a small contribution also exist in the the third harmonic range of the wave peak frequency around 0.3 Hz (not visible in linear scale). This is due to the product $u|u|$ in the drag force (see (7)), which introduces forcing in the third harmonic frequency range but not in the second harmonic range.

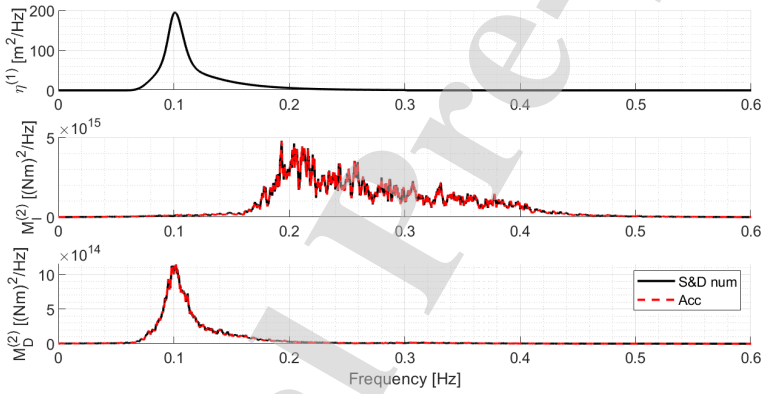

Figure 4: Spectra of first-order free-surface elevation and second-order inertia and drag moment for a 3-hour irregular sea state and 8 effective modes.

5.2. *Second-order free surface elevation*

The method can also be applied for the free surface elevation. The first-order result is stated in (18)–(19), while at second order, the result occur by substitution of the second-order potential (34) into the linear term and the first-order potential (16) into the quadratic terms of (6). We express the final result as

$$\frac{\eta_2}{h} = \sum_{m=-N}^{N} \sum_{n=-N}^{N} \hat{\tilde{B}}_m \hat{\tilde{B}}_n \mathcal{T}_\eta \mathrm{e}^{\mathrm{i}((\omega_m+\omega_n)t-(k_m+k_n)x)} + \frac{C}{gh} \tag{66}$$

where the last term serves to impose that $\bar{\eta}_2 = 0$ and where

$$\mathcal{T}_\eta = (\Omega_m + \Omega_n)\,\mathcal{T}_\Phi + \tfrac{1}{2}\kappa_m\kappa_n - \tfrac{1}{2}\Omega_m^2\Omega_n^2 - \tfrac{1}{2}\Omega_m\Omega_n\left(\Omega_m^2 + \Omega_n^2\right). \tag{67}$$

It turns out, though, that this quadratic transfer function is less suited for the eigen decomposition, showing a slow convergence with respect to the needed number of modes. This will be detailed in section 6. Good convergence properties, however, were found for the computation of $\eta_{2,t}$

$$\frac{\eta_{2,t}}{\sqrt{gh}} = \sum_{m=-N}^{N} \sum_{n=-N}^{N} \hat{\hat{B}}_m \hat{\hat{B}}_n \mathcal{T}_{\eta_t} \mathrm{e}^{\mathrm{i}((\omega_m+\omega_n)t-(k_m+k_n)x)} \tag{68}$$

through the following transfer function

$$\mathcal{T}_{\eta_t} = (\Omega_m + \Omega_n)\, \mathcal{T}_\eta. \tag{69}$$

Once $\eta_{2,t}$ is known, η_2 can be obtained by time integration in the frequency domain.

6. Eigenvalues, eigenvectors and interaction kernels

The accuracy of the method rests on the diminishing size of the eigenvalues. Hence, in the following, we investigate the behaviour of the eigenvalues, eigenvectors and QTF functions. We here collect the quadratic transfer functions into their intertia and drag parts, corresponding to the summations in (43)–(44) and (56)–(57). We use a cylinder diameter of $D = 8$ m throughout.

Figure 5 shows the decay of the eigenvalues, normalized with the first eigenvalue for each of the transfer functions. The eigenvalues related to the drag load QTFs (dot symbols) decay rapidly, and only 8 modes are needed to reach a level of $1 \cdot 10^{-14}$. For the inertia force and the $\eta_{2,t}$ QTFs (red crosses and triangles) the decay is slower, with 45 modes needed before achieving this level. The inertia moment QTF (blue crosses) has the slowest decay of the eigenvalues, with a value of $3 \cdot 10^{-3}$ for the eighth eigenvalue. Also the eigenvalues of the direct QTF for η_2 (67) are shown (circle symbols) and it can be seen that the eigenvalues reach a constant level of around $8 \cdot 10^{-3}$ after 15 modes, with no further decay. For this reason, the $\eta_{2,t}$-based approach was chosen instead, with similar convergence properties as the inertia force.

The double sided QTF functions are shown in figure 6 with the exact QTF in the left column and the ratio between the eight-mode approximation and the exact function in the middle column. For the inertia force and free surface elevation, the QTFs are quite flat, with only limited variation away from the diagonal. This is in line with the suggestion of Taylor et al. (2007) for the QTF of the full diffraction solution for a four-column structure. The largest error for the inertia force occur close to the anti-diagonal (low frequency forcing) and has a value of 0.3%. For the free surface elevation, the largest error appear to be around 3%, again at very low frequencies. The transfer functions related to the drag force are not very flat, but are approximated to full precision with 8 modes, consistent with the eigenvalue analysis of figure 5. Finally, for the inertia moment, errors up to 1.5% occur in certain bands of superharmonic interaction.

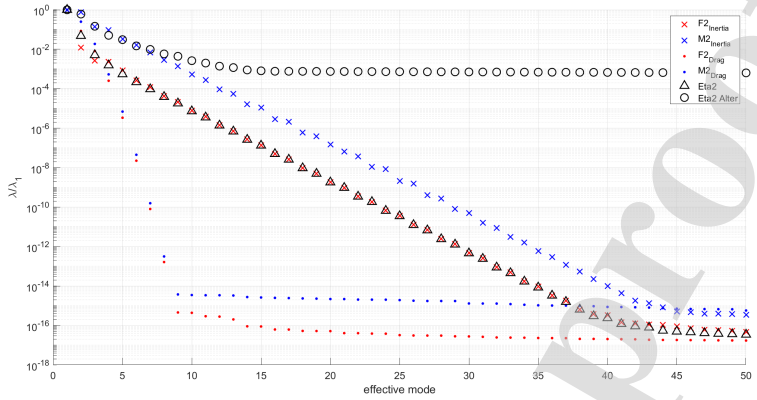

Figure 5: The eigen values for the quadratic transfer functions.

It should be noted here, however, that the mudline moment is dominated by the contribution of $F_2 h$ such that this signal has a smaller error.

The right column of the figure shows the eigen vectors for the first four effective modes. It can be seen that the eigenvectors are smooth functions of the dimensionless frequency Ω. This enables the computation on a coarse frequency grid and subsequent interpolation to finer frequency vectors of long time series. Unless other is stated, all calculations with the new method in the paper are done with 8 effective modes, calculated on a 16×16 grid in the (Ω, Ω) space and with subsequent interpolation to the full frequency resolution.

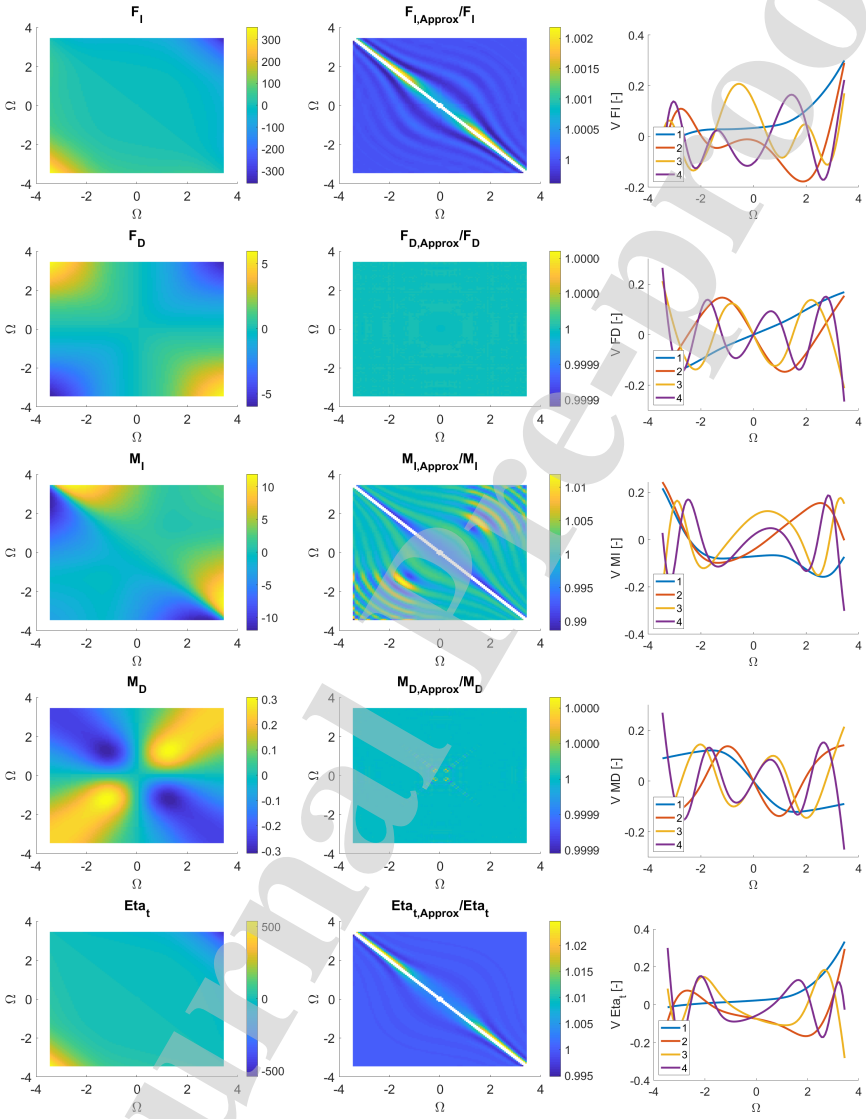

Figure 6: The quadratic transfer functions (left column) for inertia force, drag force, inertia moment, drag moment and η_t. The middle column shows the ratio of the approximate transfer function with 8 effective modes to the exact transfer function. The right column shows the eigen vectors for the first 4 effective modes.

7. Accuracy and efficiency for long time series

Following the eigenvalue analysis, we test the method's accuracy and efficiency on long time series of irregular waves. First, a 3-hour realization of an irregular sea state with 10 m significant wave height and 10 s peak period was carried out. This is the same sea state as used in figure 3–4 and is a rather strong sea state with the largest waves close to the breaking limit. Although second-order theory may thus be stretched here with respect to validity, the assessment of the new methods accuracy will not be affected, since the accuracy measures are presented in normalized format.

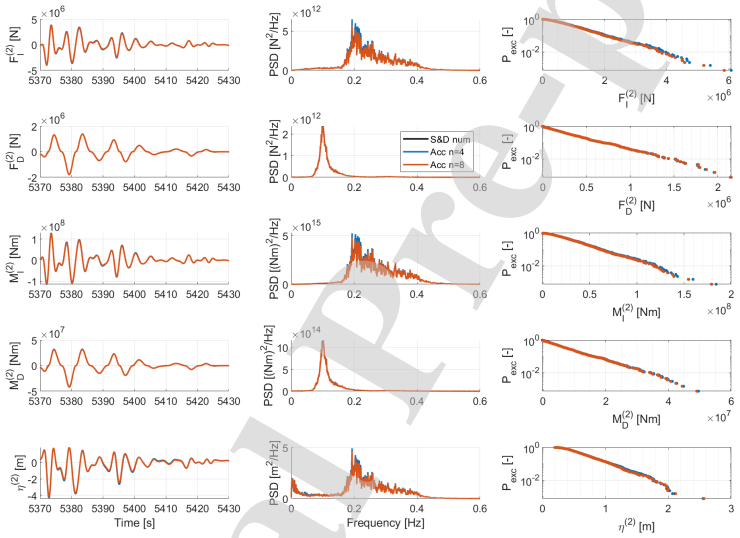

Figure 7: Second-order forces, moments and free-surface elevation for a 3-hour sea state. Time series (left), spectra (middle) and exceedance probability (right) plots.

Time series, spectra and exceedance probability plots obtained with 4 and 8 modes are compared to the Sharma & Dean solution in figure 7. The exceedance probability plots were obtained through a zero down-crossing analysis of the full first- plus second-order free surface elevation signal, such that one second-order peak value was taken out for each wave. From the spectra and exceedance probability plots, the method provides results of good accuracy for both the depth-integrated forces, the moments and the free surface elevation. Some discrepancies are observable in the exceedance probability plots, owing to the results with four modes, while the results with eight modes appear to be accurate.

The contribution of the inertia and drag components to the total loads for the specific irregular sea state of figure 7 has been quantified as well. For both

force and moment, table 1 shows the standard deviation of the total signal, σ_{tot}, as well as the standard deviation of the linear, second-order inertia and drag contributions, normalized by σ_{tot}. The drag contribution is the smallest of the three and confirms that the loads are inertia-dominated.

	σ_{tot}	$\sigma^{(1)}/\sigma_{tot}$	$\sigma_I^{(2)}/\sigma_{tot}$	$\sigma_D^{(2)}/\sigma_{tot}$
Force	2.45 MN	0.953	0.281	0.110
Moment	5.31 MNm	0.912	0.391	0.116

Table 1: Contributions of linear, second-order inertia and drag loads to the total force and moment.

A deeper analysis is now made with an error measure. We quantify the non-dimensional error in a given signal x compared to a reference signal x_{ref} by

$$err = \frac{|\max(x) - \max(x_{\text{ref}})|}{\sigma(x_{\text{ref}})}, \tag{70}$$

where σ indicates standard deviation. This is a rather demanding measure, since it is based on the distinct maxima in the two time series compared. It is stricter than the relative error, since we normalize with the standard deviation of the reference signal rather than its maximum value. From the exceedance probability plots of figure 7, this error, though, is meaningful due to the high accuracy of the method. For this purpose, we further introduce an exact reference solution, obtained by calculation with the closed-form expressions of the QTF functions of Sections 4–5. This method corresponds to retaining all modes of the eigen decomposition, but is calculated by double summation over the full set of frequency pairs, collection of the resulting Fourier amplitudes and inverse FFT transformation to the final time series.

We first assess the error of the accelerated method compared to the exact reference solution. The error for the main five second-order signals as a function of the number of modes is presented in figure 8.

We see that the error level decreases monotonously with the number of modes. The average slope corresponds to an error behaviour of roughly $err \sim \mathcal{N}^{-4.5}$ where $\mathcal{N}$ is the number of effective modes. Thus the error will decrease by a factor of around 20 if the number of effective modes is doubled. For eight modes, the error level is below 1% for all the load signals, and 1.3% for the free surface elevation. This number of modes thus seem to provide a good compromise between accuracy and numerical effort. The errors of the Sharma and Dean load method, integrated numerically with 40 points over the vertical, are also presented as dashed lines. The error is between 0.2% and 1% and it can be seen that the accuracy of the approximate method is superior when the number of modes exceeds 8.

We next investigate if the error varies across various peak wave periods or peak wave lengths. To this end, the error for the main five second-order signals as a function of $k_p h$ was computed, where h is the water depth and k_p is the wave number at the peak frequency of the wave spectrum. The results, obtained with eight modes and for a 3-hour realization, are shown in figure 9.

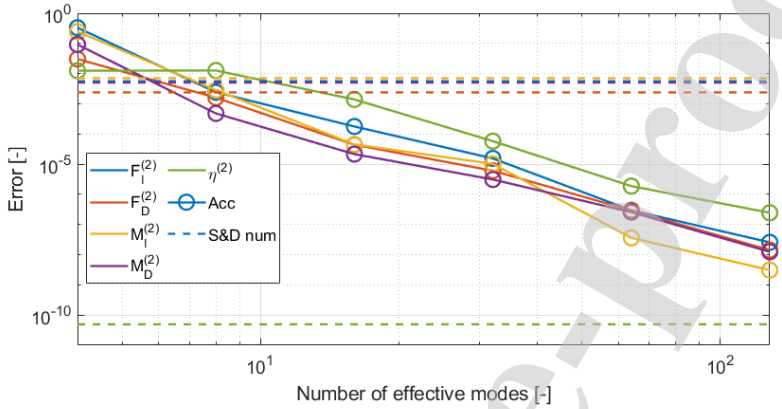

Figure 8: Error sensitivity to the number of effective modes for a 3-hour sea state. Accelerated (solid lines) and Sharma & Dean with 40 integration points (dashed).

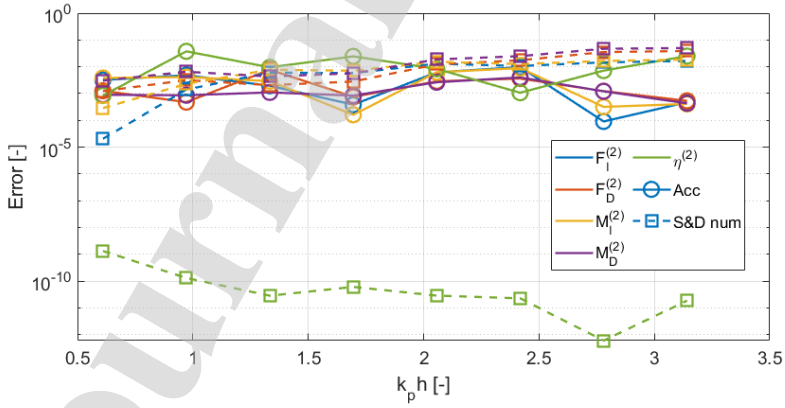

Figure 9: Error sensitivity to the wave peak period for a 3-hour sea state. Accelerated with 8 modes (solid lines) and Sharma & Dean with 40 integration points (dashed).

The error level for the accelerated method is seen to be fairly constant, and always below 1% for the loads. For the free surface elevation, the largest error of 3.8% occurs at $k_p h = 0.97$. For the numerically integrated results of the classical Sharma and Dean, the error for the loads are slightly larger and increases with $k_p h$. This is due to the concentration of the wave kinematics and loads around the still water level for increasing kh, which decreases the effective resolution of the numerical integration.

It is also interesting to check if the error depends on the simulation length. This can be seen as a test of the interpolation of the eigenvector functions, which were computed with a resolution of 16 frequencies. The error is presented in figure 10 and shows no systematic dependence to the time series length. For all simulation times, the error level is below 1%.

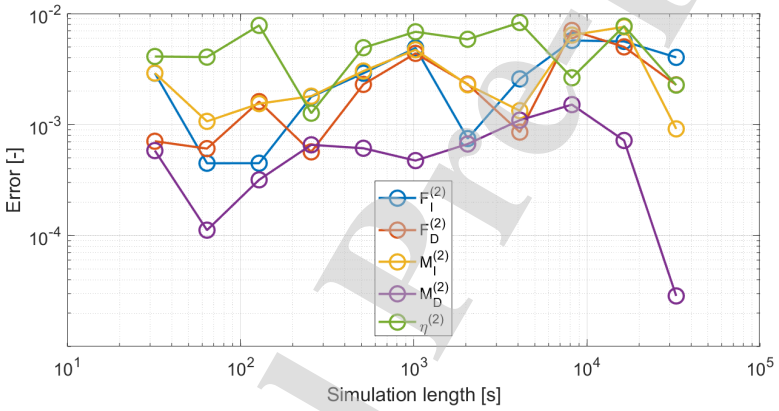

Figure 10: Error sensitivity to the simulation length. Accelerated with 8 modes.

We finally turn to the numerical efficiency of the method. The execution times for the different simulation lengths are shown in figure 11. The numerically integrated version of the Sharma and Dean method shows a scaling proportional to N^2, although with some leaning towards $O(N^3)$ for the longest simulation lengths. From the results in the figure, a 3-hour realization is obtained in 680 s with this method. The exact method with analytical depth integration also scales with N^2 and is naturally more efficient, with a 3-hour realization effort of 34 s. This is 20 times faster than for the depth integration, and we note that an additional factor of 2 could have been gained if the symmetry properties of the QTFs had been used, as is the case in our Sharma and Dean implementation. The time saving of analytical depth integration is thus consistent with the choice of 40 integration points over the depth. Finally, the accelerated method is seen to scale as $O(N \log N)$ with an execution time of 0.24 s for a 3-hour realization, which is more than 2500 times faster than for the numerical Sharma and Dean implementation. The scaling behaviour of $O(N \log N)$ starts around 2000 s, where the FFT operations begin to dominate

the initial effort of eigendecomposition. The new method is seen to be faster than the numerical Sharma and Dean for all durations tested.

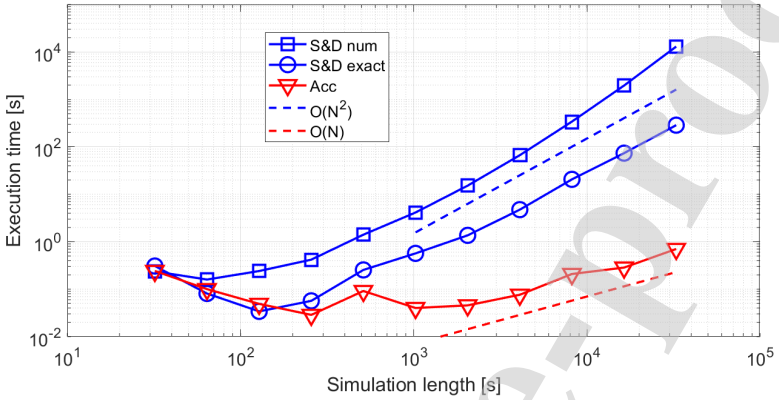

Figure 11: Execution time as a function of simulation length for the different methods.

8. Summary and conclusions

An accelerated method for the calculation of second-order monopile wave loads has been developed, based on second-order Stokes theory and the force model of Rainey (1995) plus the standard Morison drag load term. The computional effort scales as $O(N \log N)$ where N is the number of linear wave frequencies. This is one order of magnitude faster than the conventional method, that involves computation over all pairs of frequencies and thus scales as $O(N^2)$.

The numerical efficiency is achieved through i) compact double-sided Fourier series representation of the first-order wave field; ii) closed-form analytical depth integration; iii) eigenvalue decomposition of the quadratic transfer functions with modal truncation; iv) interpolation within the resulting eigenvectors and v) multiplication of pseudo time series obtained by FFT where the eigenvectors serve as transfer functions.

The method accuracy is adjustable through the number of effective modes. For eight modes, an accuracy of 1% for the largest value of the second-order loads within a three hour event was obtained, relative to the standard deviation of the signal. This error level is superior to the classical Sharma and Dean method with depth integration along 40 points in the vertical, but could be obtained at 0.24 s, which is 2500 times faster. The dependency of the load error level to the number of effective modes has further been investigated and was found to decrease roughly as $\mathcal{N}^{-4.5}$, where $\mathcal{N}$ is the number of effective modes. Next, the dependency to $k_p h$ and simulation length was investigated, and the error bound of 1% for the largest peak load value was found to hold, with no systematic variation to these two parameters. For the second-order free surface

elevation, the Sharma and Dean method is identical to the exact and the largest peak error was 3.8% with the new method at eight effective modes. This can be reduced by increase of the number of modes.

The ability to compute a 3-hour second-order load time series in 0.24 s has wide perspectives in Engineering design. It may potentially enable second-order analysis to be included in design in the same role that linear load computations are utilized today. While the present derivation is limited to vertical cylinders and unidirectional waves, the extension to more general geometry and wave-current fields is part of our current research. The method of eigenvalue decomposition and subsequent FFT-based calculation can also be applied to QTF results of radiation-diffraction methods, although the speed-up will only apply to the time series realizations and not to the initial radiation-diffraction analysis.

Besides the more accurate peak load prediction relative to linear wave theory, the second-order load theory also adds forcing at frequencies outside the linear wave spectrum through the sub- and super harmonic forcing. This has importance for resonance effects for monopile wind turbines and also to the low-frequency forcing of floating wind turbines. A pilot study with response calculations for a spar floater has been presented by Pegalajar-Jurado and Bredmose (2020). Further steps in this direction will be the incorporation into floating substructure design, where the efficiency of the present method enables its use in optimization studies, in which several fast realizations are evaluated by an optimizer.

Acknowledgement

This work was carried out as part of the FloatStep project, funded by Innovation Fund Denmark under grant no. 8055-00075B. This support is gratefully acknowledged. Discussions with Prof. Harry Bingham, DTU, are gratefully acknowledged too.

References

Bredmose, H., Agnon, Y., Madsen, P. A., Schäffer, H. A., 2005. Wave transformation models with exact second-order transfer. Eur. J. Fluid Mech. B/Fluids 24, 659–682.

Bredmose, H., Pegalajar-Jurado, A., August 2020. An $n \log n$ method for second-order wave loads on a vertical pile. In: 35th Int. Worshop Water Waves Floating Bodies. Seoul, South Korea (Virtual).

Bredmose, H., Schäffer, H. A., Madsen, P. A., 2004. Boussinesq evolution equations: Numerical efficiency, breaking and amplitude dispersion. Coastal Engng. 51 (11–12), 1117–1142.

Dean, R. G., Dalrymple, R. A., 1991. Water wave mechanics for Engineers and Scientists. World Scientific.

Fenton, J. D., 1985. A fifth-order Stokes theory for steady waves. J. Waterway Port Coastal Ocean Engng. 111 (2), 216–234.

Grue, J., Huseby, M., 2002. Higher-harmonic wave forces and ringing of vertical cylinders. Appl. Ocean Res. 24 (4), 203–214.

Isaacson, M., 1979. Wave-induced forces in the diffraction regime. In: Shaw, T. (Ed.), Mechanics of Wave-Induced Forces on Cylinders. Pitman Advanced Publishing Program, pp. 68–89.

Kim, M., Chen, W., 1994. Slender-body approximation for slowly-varying wave loads in multi-directional waves. Appl. Ocean Res. 16, 141–163.

Kristiansen, T., Faltinsen, O. M., 2017. Ringing loads on a vertical cylinder in finite water depth. The International Workshop on Water Waves and Floating Bodies 2017 (3), 1–4.

Madsen, P., Fuhrman, D., 2006. Third-order theory for bichromatic bi-directional water waves. Journal of Fluid Mechanics 557, 369–387.

Morison, J. R., O'Brien, M. P., Johnson, J. W., Schaaf, S. A., 1950. The forces exerted by surface waves on monopiles. J. Petrol. Techn. 189, 149–154.

Newman, J., 1974. Second order slowly varying forces on vessels in irregular wave. In: Paper 19, pages 182-186 in 'The Dynamics of Marine Vehicles and Structures in Waves', ed. Bishop, R.E. and Price W.G. Publ. By I.Mech. E, London.

Pegalajar-Jurado, A., Bredmose, H., 2020. Accelerated hydrodynamic analysis for spar buoys with second-order wave excitation. In: Proceedings of the ASME 39th International Conference on Ocean, Offshore and Arctic Engineering (OMAE 2020). Online.

Pierella, F., Bredmose, H., Dixen, M., 2021. Generation of highly nonlinear irregular waves in a wave flume experiment: Spurious harmonics and their effect on the wave spectrum. Coastal Engineering 164.

Pierella, F., Lindberg, O., Bredmose, H., Bingham, H. B., Read, R. W., Engsig-Karup, A. P., 2020. The derisk database: Extreme design waves for offshore wind turbines.

Rainey, R. C. T., 1995. Slender-body expressions for the wave load on offshore structures. Proc. Roy. Soc. London Series A. Math. and Phys. Sci. 450 (1939), 391–416.

Schäffer, H. A., Steenberg, C. M., 2003. Second-order wavemaker theory for multidirectional waves. Ocean Engng. 30, 1203–1231.

Schløer, S., Bredmose, H., Bingham, H. B., 2016. The influence of fully nonlinear wave forces on aero-hydro-elastic calculations of monopile wind turbines. Marine Structures 50, 162–188.

Sharma, J., Dean, R., 1981. Second-order directional seas and associated wave forces. Socity of Petrolium Engineers Journal, 129–140.

Standing, R. G., Brendling, W. J., Wilson, D., 1987. Recent developments in the analysis of wave drift forces, low-frequency damping and response. In: Proc. of the Offshore Technology Conference (OTC). OTC, dOI:10.4043/5456-MS.

Suja-Thauvin, L., Bachynski, E., Pierella, F., Borg, M., Krokstad, J., Bredmose, H., 2020. Critical assessment of hydrodynamic load models for a monopile structure in finite water depth. Marine Structures 72.

Taylor, P., Zang, J., Walker, D., Taylor, R., 2007. Second-order near-trapping for multi-column structures and near-flat qtfs. In: Proceedings of the 22nd Int. Workshop Water Waves Floating Bodies. Plitvice, Croatia.

Tromans, P. S., Anaturk, A., Hagemeijer, P., Edinburgh, UK, 11–16 August 1991. A new model for the kinematics of large ocean waves — application as a design wave. In: Proc. 1st Int. Conf. Offsh. Mech. and Polar Engng. (ISOPE). Vol. 3. pp. 64–71.

Walker, D., Taylor, P., Taylor, R. E., 2004. The shape of large surface waves on the open sea and the draupner new year wave. Applied Ocean Research 26 (3), 73 – 83.
URL http://www.sciencedirect.com/science/article/pii/S0141118705000052

Wang, S., Larsen, T., Bredmose, H., 2021. Ultimate load analysis of a 10 mw offshore monopile wind turbine incorporating fully nonlinear irregular wave kinematics. Submitted for publication.

Appendix A. Expressions for arbitrary vertical span

We here give results for a vertical cylinder with arbitrary locations of the lower and upper end z_1, z_2. The monopile can be seen as a special case of this with $z_1 = -h, z_2 = 0$. We note that the surface force and its moment F_{24}, M_{24} should only be included if the cylinder pierces through the still water level.

We write the linear force as

$$\mathcal{F}_1 = \frac{\Omega}{\cosh\kappa}\left[\sinh\left(\kappa(Z+1)\right)\right]_{Z_1}^{Z_2} \tag{A.1}$$

and obtain the quadratic transfer function from the second-order Eulerian acceleration similarly as

$$\mathcal{F}_{21} = \mathcal{T}_\phi \frac{\Omega_m + \Omega_n}{\cosh(\kappa_m + \kappa_n)}\left[\sinh\left((\kappa_m + \kappa_n)(Z+1)\right)\right]_{Z_1}^{Z_2} \tag{A.2}$$

The transfer functions $\mathcal{F}_{22} - -\mathcal{F}_{25}$ can be written in the same format as (50)–(55), but with modified values of the integrals IF_1–IF_2 that takes the arbitrary

integration limits into account:

$$\mathrm{IF}_1 = \frac{1}{h}\int_{z_1}^{z_2} \cosh k_m(z+h)\cosh k_n(z+h)\ \mathrm{d}z = \frac{1}{2}\left[C_1 + C_2\right]_{Z_1}^{Z_2} \tag{A.3}$$

$$\mathrm{IF}_2 = \frac{1}{h}\int_{z_1}^{z_2} \sinh k_m(z+h)\sinh k_n(z+h)\ \mathrm{d}z = \frac{1}{2}\left[C_1 - C_2\right]_{Z_1}^{Z_2} \tag{A.4}$$

and where

$$C_1 = \frac{\sinh\left(\left(\kappa_m + \kappa_n\right)(Z+1)\right)}{\kappa_m + \kappa_n} \quad , \quad C_2 = \frac{\sinh\left(\left(\kappa_m - \kappa_n\right)(Z+1)\right)}{\kappa_m - \kappa_n}. \tag{A.5}$$

Here we have further defined $Z \equiv z/h$. For C_1 and C_2, the asymptotic limit of $Z+1$ must be applied for the case when the denominator is equal to zero.

For the linear moment, the changed integration limits leads to

$$\mathcal{M}_1 = \frac{\Omega}{\cosh\kappa}\left[Z\sinh\kappa(Z+1) - \frac{1}{\kappa}\cosh\kappa(Z+1)\right]_{Z_1}^{Z_2}. \tag{A.6}$$

The quadratic transfer function for the moment of the second-order Eulerian acceleration is obtained in the same was as

$$\mathcal{M}_{21} = \mathcal{T}_\phi \frac{\Omega_m + \Omega_n}{\cosh(\kappa_m + \kappa_n)} \tag{A.7}$$

$$\times\left[Z\sinh(\kappa_m+\kappa_n)(Z+1) - \frac{1}{(\kappa_m+\kappa_n)}\cosh(\kappa_m+\kappa_n)(Z+1)\right]_{Z_1}^{Z_2}. \tag{A.8}$$

Next, for $\mathcal{M}_{22}$–$\mathcal{M}_{25}$, the expressions (63)–(65) also hold, but with modified expressions for the vertical integrals. Here we get

$$\mathrm{IM}_1 = \frac{1}{h^2}\int_{z_1}^{z_2} \cosh k_m(z+h)\cosh k_n(z+h)\ z\ \mathrm{d}z \tag{A.9}$$

$$= \frac{1}{2}\left[Z\left(C_1 + C_2\right) - \left(C_3 + C_4\right)\right]_{Z_1}^{Z_2} \tag{A.10}$$

$$\mathrm{IM}_2 = \frac{1}{h^2}\int_{-z_1}^{z_2} \sinh k_m(z+h)\sinh k_n(z+h)\ z\ \mathrm{d}z \tag{A.11}$$

$$= \frac{1}{2}\left[Z\left(C_1 - C_2\right) - \left(C_3 - C_4\right)\right]_{Z_1}^{Z_2} \tag{A.12}$$

where

$$C_3 = \frac{\cosh\left(\left(\kappa_m + \kappa_n\right)(Z+1)\right) - 1}{(\kappa_m + \kappa_n)^2} \quad , \quad C_4 = \frac{\cosh\left(\left(\kappa_m - \kappa_n\right)(Z+1)\right) - 1}{(\kappa_m - \kappa_n)^2} \tag{A.13}$$

and where again the limits $C_3 = \frac{1}{2}(Z+1)^2$, $C_4 = \frac{1}{2}(Z+1)^2$ apply when their respective denominators are equal to zero.

Second-order monopile wave loads at linear cost

H. Bredmose and A. Pegalajar-Jurado
DTU Wind Energy, Nils Koppels All_e Building 403, DK-2800 Kgs. Lyngby, Denmark

Highlights

- Fast method for second-order loads on vertical cylinders
- Method valid for force, moment and free surface elevation
- Scales like N Log N, similarly to linear wave loads
- Accuracy is adjustable
- 3 hour time series can be obtained at 0.24 s. 2500 times faster than with conventional method.

Second-order monopile wave loads at linear cost

H. Bredmose and A. Pegalajar-Jurado
DTU Wind Energy, Nils Koppels Allé Building 403, DK-2800 Kgs. Lyngby, Denmark

Author Credit Statement

H.B. developed the calculation method, the initial numerical implementation, wrote the original manuscript and contributed to the revision of the manuscript. A. P.-J. completed the code, conducted the numerical calculations, contributed to the original manuscript and revised the manuscript.

Declaration of interests

☒ The authors declare that they have no known competing financial interests or personal relationships that could have appeared to influence the work reported in this paper.

☐The authors declare the following financial interests/personal relationships which may be considered as potential competing interests: